Process based modelling of power density for wire laser additive manufacturing using a coaxial head

Clément Roch, Christophe Tournier, Sylvain Lavernhe

Process based modelling of power density for wire laser additive manufacturing using a coaxial head

Clément Roch[a], Christophe Tournier[a], Sylvain Lavernhe[a,]

[a] *Université Paris-Saclay, ENS Paris-Saclay, LURPA, 91190, Gif-sur-Yvette, France*

Abstract

Wire Laser Additive Manufacturing enables the production of near net shape parts at high deposition rates while reducing the risks due to metallic powder handling. Common configurations of this process use a single laser beam with lateral wire feeding, inducing a dependency on the feeding angle and direction relative to the travel direction. In contrast, coaxial configurations feed the wire along the direction of the energy input, which can be achieved by using a ring beam or multiple beams. In this case, the beams are placed so that they form a single spot on the focal plane. Varying the distance between the intersection point of the beams and the substrate allows for specific power densities with different spot sizes, resulting in varying bead geometries and penetrations. However, most models for process simulations consider a single equivalent beam or a single heat source to model the power input, which cannot accurately represent the obtained power densities. This article presents a modelling of power density inspired by the process for coaxial heads. The developed approach can be used to simulate the laser power density on any surface with any number of beams. It is applied to model the experimental setup using a three beam coaxial head with an identified laser beam model. The simulated power densities are compared to experimental results to validate the predictions of spot size and shape. To better represent process behaviour, both wire and bead are modelled and the power densities are simulated on these surfaces. Finally, the effect of the head rotation is investigated as it modifies the power density and geometry of the beads. The resulting power profiles are compared to the internal and external profiles of the manufactured beads to conclude on the effect of this parameter.

Keywords: Wire Laser Additive Manufacturing (WLAM), power modelling, bead geometry, penetration, laser head orientation

1. Introduction

Metal additive manufacturing offers new possibilities for the development of new production strategies. Powder based processes are the most common, but require complex installations due to the risks of powder handling. Processes using metallic wire as feedstock material show great promise as they reduce these constraints while producing solid parts with large volumes. Wire Laser Additive Manufacturing (WLAM) is one of these wire based processes using a laser beam as an energy supply, belonging to the Directed Energy Deposition (DED) category [1]. The manufacturing process consists in feeding the metallic wire towards the substrate and using the laser to melt them. As the head on which the laser and feeding system are mounted follows the programmed trajectory, the melt pool solidifies to form a welding bead. Therefore, the term bead will be used to describe the total deposited matter, including both solidified and melted zones. Layers can be built by generating adjacent welding beads, and the superposition of beads allows for manufacturing full or hollow parts [2]. The most common setup found in the literature and referred to as lateral wire feeding uses a laser beam oriented perpendicularly to the substrate and a wire supplied from the side. Other configurations place the wire axis along an equivalent laser axis, creating a coaxial setup. This can be achieved by using a ring beam [3, 4] or multiple laser beams [5, 6]. In this latter configuration the beams are often placed so that they intersect each other to form a single spot when focused on the substrate, similarly to a single laser. Varying the distance between the beams' intersection and the substrate, referred to as working distance, results in multiple spots, deviating from proper axis-symmetrical behaviour. Increasing the number of beams can homogenize the power density if all beams are properly focused, and their power properly managed, resulting in added complexity. Beam shaping is also used to obtain a ring beam from a single source but requires complex optical paths to insert the wire inside the ring.

Because the manufacturing is based on three principal elements being the feed material, the power input, and the path followed by the head, managing the interactions be-

Email addresses: clement.roch@ens-paris-saclay.fr (Clément Roch), christophe.tournier@ens-paris-saclay.fr (Christophe Tournier), sylvain.lavernhe@ens-paris-saclay.fr (Sylvain Lavernhe)

tween them is essential to achieve a stable process. Studies on lateral wire feeding linked several process defects to these parameters and highlighted the importance of the ratio between power and feed speed [7, 8]. Once a stable process is achieved, parts can be manufactured with the goal of generating near net shapes. Since these parts are created by multiple beads, controlling the bead geometry is essential for the manufacturing of complex volumes. Because of its similarity to other welding based processes, models describing single and overlapping bead geometries are shared with other processes [9]. The main models to simulate single bead geometry include elliptical [10, 11], sinusoidal [12] or polynomial equations of degree two [13, 14] or four [15]. Most of these models offer a satisfactory representation of the beads [16], with the optimal model being linked to process parameters [9]. Therefore, most studies describe bead geometries only by their dimensions and focus on the influence of process parameters on these dimensions. The available literature focuses on three main process parameters: laser power, wire feed speed, and travel speed, and shows that width and height can vary independently [17]. Some studies investigate other parameters such as wire angle and feeding direction for lateral feeding setups [18], while for coaxial configurations some investigate the effect of the working distance on the produced beads [19, 20]. For setups with multiple laser beams, this distance corresponds to the distance between the intersection point of all beams and the substrate. When this distance is null, all lasers create a single spot that can be approximated by a single laser, but when this distance increases the beams create multiple spots which differ from the single beam representation.

This effect of multiple beams interacting with the surface is rarely discussed in the literature, where most models for process simulations consider a single heat source [21]. This source is often described by Gaussian [22] or Goldak [23] models and rarely considers the power profile of the laser beam. This can lead to an overestimation of the maximal value of the power density or to an inaccurate size of the source. Moreover, the source is often applied to the geometry of the substrate to simulate the heat input, while process observations reveal that the lasers interact mostly with the wire and bead rather than the substrate. Some studies consider the bead geometry with uniform or Gaussian power sources [24, 25]. Ji et al use multiple heat sources on the bead geometry to account for the different beams, but the model for laser power is based on planar surfaces and therefore does not account for how the bead geometry modifies the power density [20]. The power input on the wire is mostly considered negligible, with an analytical model to describe its thermal behaviour for an annular Gaussian beam proposed by Cazaubon [26].

This study presents a novel approach to simulate power density in WLAM process based on a realistic modelling of the power source and of the in-process geometry. The power density of the beams is represented by super-Gaussian (SG) functions to correspond to near top-hat profiles. The proposed method can simulate the power density for a multiple beams head on complex surface geometries, including substrate, bead, and wire. Furthermore, the head position relative to the workpiece or substrate is taken into account to characterize the effect of the orientation parameters on power density. The laser irradiance simulation on any surface is first introduced before discussing the associated laser model based on beam measurements. The experimental setup uses a coaxial head from Coaxworks with three top-hat beams (figure 1), and an associated model with three identified SG beams is proposed and compared to experimental results for spot prediction. The simulation of power density on any surface is then applied to the wire and bead to better represent the in-process behaviour. To investigate whether the head rotation impacts the produced beads, several beads are produced and differences in geometries and penetrations are observed. Simulations on measurements of the experimental beads profiles are then used to link the power density profiles to the internal and external geometries of the beads. While the presented work is applied to a coaxial head with three beams and top-hat profiles, the developed approach is suited to any number of beams and can be adapted to various power profiles and ring beams.

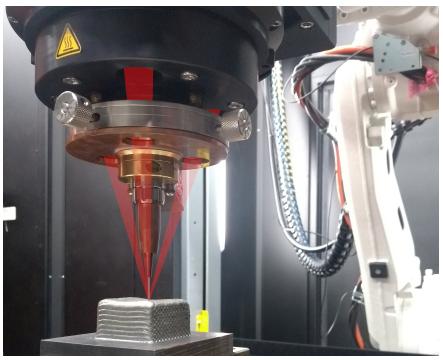

Figure 1: Experimental setup with the Coaxworks coaxial head, the paths of the three laser beams are represented in red

This paper presents the usual models for laser beams and the method used to simulate the power on any surface in section 2. Section 3 describes the identified laser profile, and compares the simulated laser spots to experimental results. Section 4 details how the wire and bead are modelled and integrated into the simulation. The effect of the head rotation on the bead geometries and the power density is presented in section 5 before concluding in section 6.

2. Laser power simulation

The developed method enables the simulation of the laser power density on any surface for a multiple beams head. The structure of this method is presented in Fig. 2, and the following sections detail the necessary steps for the power simulation on any surface.

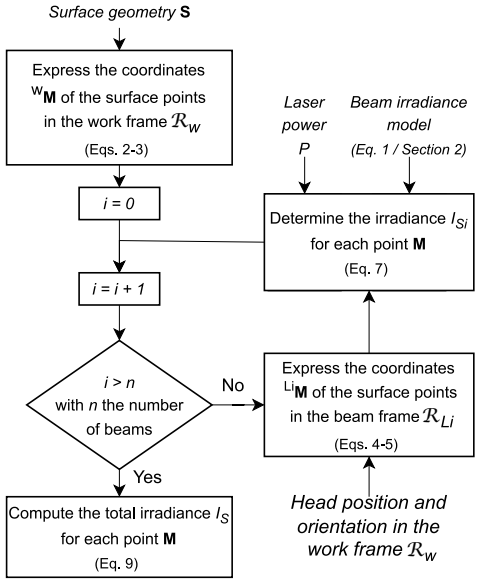

Figure 2: Flowchart of the developed method for irradiance simulation with multiple beams

2.1. Models of power sources

Modelling the input power as an equivalent heat source is insufficient to describe the process with multiple beams or to take into account the geometries of the bead and wire. Moreover, the Gaussian heat source model is well adapted to laser beams with Gaussian energy distribution profiles, which are not the only beams available. Therefore some studies focus directly on laser power, enabling a finer modelling of the beams profile [27]. The power density, described by the irradiance I in $(\mathrm{kW/mm^2})$ is linked to the melting behaviour [28, 29, 30] and is sometimes used to describe the process [31]. The evolution of the irradiance I along the axis of propagation z and the cross-section axis r serves as a model of the laser beam. Fig. 3 illustrates the evolution of the beam size w along z for a Gaussian beam, with the minimum value obtained in the focal plane ($z = 0$). The irradiance profiles at the focal plane and other beam cross-sections are presented underneath, showing the Gaussian distribution and the decrease in the irradiance value at the centre when z increases.

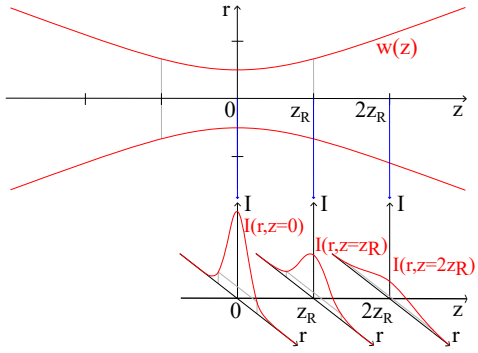

Figure 3: Size variation and irradiance profiles of a Gaussian laser beam

While this figure represents a Gaussian beam, other profiles are used in laser processes, such as the ideal top-hat profile, which presents a uniform irradiance across r and z [24]. In practice, top-hat beams are only uniform on the focal plane and tend to revert to a Gaussian profile the further z is from the focal point. Super-Gaussian (SG) functions can be used to model this evolution (Eq. 1) with k the order of the SG, $I_m(z)$ and $w(z)$ the maximal irradiance and beam width for the axial distance z.

$$I(r,z) = I_m(z)e^{-2\left(\frac{r}{w(z)}\right)^k} \tag{1}$$

For $k = 2$ the expression corresponds to a Gaussian function, therefore the SG can be described as a generalization of the Gaussian function with different orders allowing to transition from a Gaussian to a top-hat profile (Fig. 4). The following concepts in this section will be illustrated with a Gaussian beam as it is later generalized for SG beams.

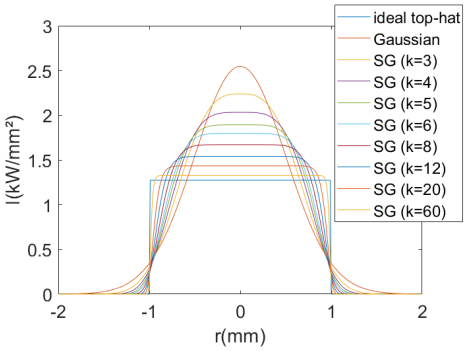

Figure 4: Comparison between different orders of Super-Gaussian (SG), top-hat and Gaussian profiles

2.2. Estimated power on a surface

The coordinates of any point $\mathbf{M}$ on a surface $\mathbf{S}$ and its associated normal $\mathbf{n}_{\mathrm{S,M}}$ can be expressed in the work frame $\mathcal{R}_W$ as follows:

$$^{\mathrm{W}}\mathbf{M} = \begin{bmatrix} ^{\mathrm{W}}x_{\mathrm{M}} \\ ^{\mathrm{W}}y_{\mathrm{M}} \\ ^{\mathrm{W}}z_{\mathrm{M}} \end{bmatrix} \tag{2} \qquad ^{\mathrm{W}}\mathbf{n}_{\mathrm{S,M}} = \begin{bmatrix} ^{\mathrm{W}}u_{\mathrm{M}} \\ ^{\mathrm{W}}v_{\mathrm{M}} \\ ^{\mathrm{W}}w_{\mathrm{M}} \end{bmatrix} \tag{3}$$

For n identical lasers, the irradiance due to each beam $\mathrm{L}_i, i \in [\![1\ ,\ n]\!]$ is computed knowing the point coordinates in the beam frame. Homogeneous coordinates are used to compute these coordinates and two transformation matrices are used to link the laser, head, and work frame: $^{\mathrm{Li}}\mathbf{T}_{\mathrm{H}}$ from each beam frame $\mathcal{R}_{Li}$ to the head frame $\mathcal{R}_H$, $^{\mathrm{H}}\mathbf{T}_{\mathrm{W}}$ from the head frame $\mathcal{R}_H$ to the work frame $\mathcal{R}_W$. $^{\mathrm{H}}\mathbf{T}_{\mathrm{W}}$ depends on the position and orientation of the head to the part and is therefore variable, depending on the programmed trajectory, while $^{\mathrm{Li}}\mathbf{T}_{\mathrm{H}}$ only depends on head technology and remains constant. The composition between frames leads to the following expressions:

$\forall\, i \in [\![1\ ,\ n]\!], \forall\, \mathbf{M} \in \mathbf{S}$:

$$ {}^{\mathrm{Li}}\mathbf{M} = \begin{bmatrix} {}^{\mathrm{Li}}x_{\mathrm{M}} \\ {}^{\mathrm{Li}}y_{\mathrm{M}} \\ {}^{\mathrm{Li}}z_{\mathrm{M}} \\ 1 \end{bmatrix} = {}^{\mathrm{Li}}\mathbf{T}_{\mathrm{H}} \cdot {}^{\mathrm{H}}\mathbf{T}_{\mathrm{W}} \cdot \begin{bmatrix} {}^{\mathrm{W}}x_{\mathrm{M}} \\ {}^{\mathrm{W}}y_{\mathrm{M}} \\ {}^{\mathrm{W}}z_{\mathrm{M}} \\ 1 \end{bmatrix} \tag{4} $$

$$ {}^{\mathrm{Li}}\mathbf{n}_{\mathrm{S,M}} = \begin{bmatrix} {}^{\mathrm{Li}}u_{\mathrm{M}} \\ {}^{\mathrm{Li}}v_{\mathrm{M}} \\ {}^{\mathrm{Li}}w_{\mathrm{M}} \\ 0 \end{bmatrix} = {}^{\mathrm{Li}}\mathbf{T}_{\mathrm{H}} \cdot {}^{\mathrm{H}}\mathbf{T}_{\mathrm{W}} \cdot \begin{bmatrix} {}^{\mathrm{W}}u_{\mathrm{M}} \\ {}^{\mathrm{W}}v_{\mathrm{M}} \\ {}^{\mathrm{W}}w_{\mathrm{M}} \\ 0 \end{bmatrix} \tag{5} $$

Given that each beam propagates along the $-\mathbf{z}$ axis of its $\mathcal{R}_{Li}$ frame, the angle θ between a beam axis and the surface normal can be expressed by Eq. 6. The irradiance I_{Si} received by a point $\mathbf{M}$ of $\mathbf{S}$ from the beam L_i can then be expressed by Lambert's law and Eq. 1, resulting in Eq. 7 with $v_i = 1$ if the point is visible by the laser, and 0 otherwise (section 4.1).

$$ \theta\left(\mathbf{n}_{\mathrm{S,M}}, \mathbf{z}_{Li}\right) = \cos^{-1}\left({}^{\mathrm{Li}}w_{\mathrm{M}}\right) \tag{6} $$

$$ I_{Si}(\mathbf{M}) = I\left(r_M, {}^{\mathrm{Li}}z_{\mathrm{M}}\right) \cdot \cos\left(\theta\left(\mathbf{n}_{\mathrm{S,M}}, \mathbf{z}_{Li}\right)\right) \cdot v_i \tag{7} $$

with

$$ {r_{\mathrm{M}}}^2 = {}^{\mathrm{Li}}{x_{\mathrm{M}}}^2 + {}^{\mathrm{Li}}{y_{\mathrm{M}}}^2 \tag{8} $$

Using this method it is possible to simulate the irradiance on any surface for each beam (Fig. 5a). Under the hypothesis that the laser beams do not influence one another, the total irradiance I_S perceived by a point is considered equal to the sum of each beam irradiance (Fig. 5b):

$$ I_S(\mathbf{M}) = \sum_{i=1}^{n} I_{Si}(\mathbf{M}) \tag{9} $$

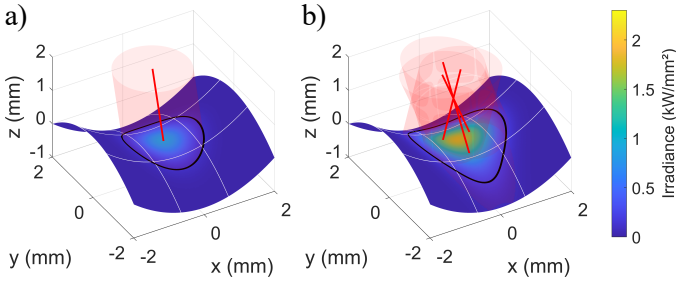

Figure 5: Simulation of the laser power on a surface for a single and multiple beams

Considering the three beams instead of only one results in different power densities on the surface. The black lines in Fig. 5 represent the contours of the laser spot, as defined in the following section. The obtained spots differ significantly between the single and multiple beams models, as the latter results in a wider and less circular shape.

2.3. Laser spot

As seen in Fig. 5, the entire surface isn't significantly impacted by the laser, with areas receiving little to no irradiance. Detecting the limits of the affected zone is useful for process simulation as it identifies the geometries with which the beams interact and the size of this zone. This limit will be referred to as the laser spot and can be defined by multiple criteria, with two of the most usual being the $1/e^2$ and D86, corresponding respectively to a threshold value and an included power criteria [32]. However, they are defined for orthogonal cross-sections of a laser profile, and not for multiple beams on non planar surfaces. A modified definition of the D86 criterion, corresponding to the irradiance threshold for which a given percentage of the total power is included inside the spot, is used to define the contour with three laser beams on any surface and for any position of the head (Fig. 5). Fig. 6 shows the three laser axes and laser spot shapes for working distances in the interval $[-5; +5]$ mm, as well as the power density obtained on planes for some of these distances. This clearly illustrates the interest of a three beams model compared to a single beam when the working distance is different from zero, which is often the case as a negative working distance is used to obtain wider beads.

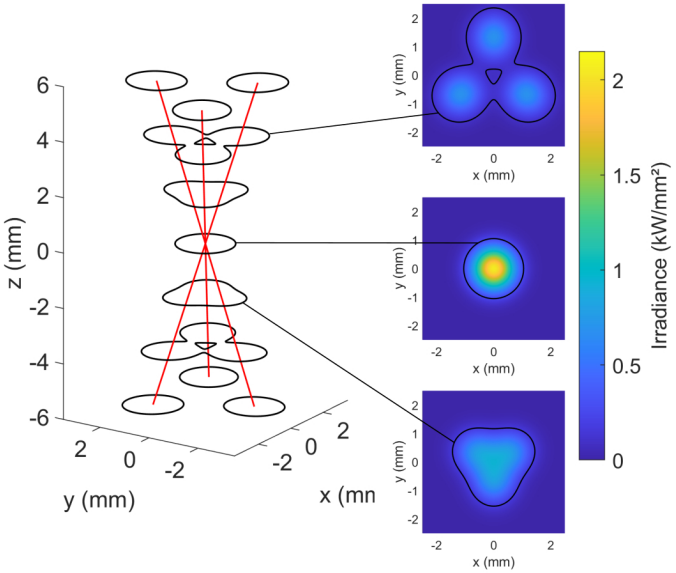

Figure 6: Shape of the laser spot and power distribution for different working distances

3. Comparison with experimental results

3.1. Laser beam identification

To better represent the laser beam before the head, an identified SG model is proposed based on beam measurements. These include measurements of the output power using a PRIMES PowerMonitor (PM48) and of the intensity profile using a PRIMES FocusMonitor (FM+). They were performed for the laser beam emitted by the source, an IPG YLS-4000, with a simple lens mounted at the end of the optical fibre. Therefore, these measurements do not take into account the optical characteristics of the laser head, nor the multiple beams behaviour. The data obtained corresponds to power profiles for 41 planes across

40 mm of the **z** axis with a power of 4 kW. The observed power density is very similar to an ideal top hat when close to the focal plane and a Gaussian profile when further away (Fig. 7). Therefore, a single continuous function of top-hat or Gaussian form is not sufficient to describe the evolution of power density for all z values. Moreover, the profiles present a decrease in power density in the beam center. To describe these profiles, a SG model is used with a subtraction of a Gaussian to represent the density loss near the centre of the beam (Eqs. 10-11). The irradiance is considered to be proportional to the total laser power P.

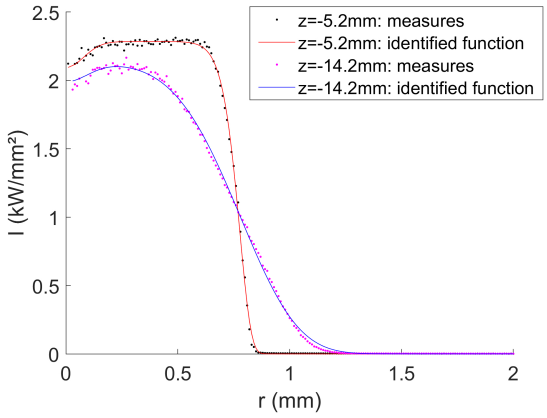

Figure 7: Measured irradiance and proposed model for $z = -5.2$ mm and $z = -14.2$ mm

$$I(r,z) = P \cdot I_m(z - z_0)\, exp\left(-2\left(\frac{r}{w(z-z_0)}\right)^{k(z-z_0)}\right) - P \cdot I_c(r, z - z_0) \quad (10)$$

$$I_c(r,z) = c_0 \frac{c_1^2}{c_1^2 + z^2}\, exp\left(-2\frac{r^2}{c_2\left(1 + \frac{z}{c_1}^2\right)}\right) \quad (11)$$

To obtain a model of the laser beam for each r and z value, the function described before is identified for each cross-section. This leads to 41 values of I_m, w, and k. A theoretical function defining the width for each z value is known for Gaussian beams and is used as a basis to describe the evolution of w for this beam. Polynomial terms are added to fit more closely the almost linear behaviour observed for high z values. The evolution of k along z presents a Gaussian shape, which corresponds to an almost top-hat profile near the focal plane (high value of k) and a more Gaussian power profile far from the focal plane ($k \approx 2$). While a theoretical function for I_m could be proposed in order to maintain the total power inside the beam, polynomial functions were chosen to match the evolution of I_m, with a fourth degree suiting the measured data. The proposed functions to describe the characteristic values are as follows:

$$w(z) = a_w \sqrt{1 + \left(\frac{z}{b_w}\right)^2} + c_w \cdot z + d_w \quad (12)$$

$$k(z) = a_{k,1}\, e^{-\left(\frac{z}{b_{k,1}}\right)^2} + a_{k,2}\, e^{-\left(\frac{z}{b_{k,2}}\right)^2} + c_k \quad (13)$$

$$I_m(z) = \sum_{j=1}^{m} a_j \cdot z^j \quad (14)$$

Once all the functions describing the shape of the laser beam are defined, an optimization using least mean squares method identifies all of the parameters. The values for each parameter obtained by this method are listed in table 1, and the resulting power distribution is displayed in Fig. 8. The colors in this figure correspond to the absolute difference between the measured data and the proposed model. One can observe that these differences stay inferior to 0.15 kW/mm^2 everywhere except near the focal plane, where the variations in intensity are the highest. Because the optimization did not impose any constraints on the total power of the laser beam, the total power for each of the forty-one planes is evaluated and the variation for this model exceeds that of the measurement, while never exceeding 4% of variation to the nominal power. Therefore, this model can be considered as representative of the laser beam, and the head will be described by three lasers of the identified shape. Each beam irradiance is equal to a third

Table 1: Identified parameters for the proposed laser model

eq 10	z_0 (mm)	-2.15
eq 11	c_0 (kW/mm^2)	0.199
	c_1 (mm)	18.5
	c_2 (mm^2)	0.0230
eq 14	a_4 (kW/mm^6)	-5.00×10^{-7}
	a_3 (kW/mm^5)	-5.20×10^{-6}
	a_2 (kW/mm^4)	9.93×10^{-5}
	a_1 (kW/mm^3)	5.15×10^{-3}
	a_0 (kW/mm^2)	5.65×10^{-1}
eq 12	a_w (mm)	0.0455
	b_w (mm)	2.53
	c_w	-0.00379
	d_w (mm)	0.735
eq 13	$a_{k,1}$	6.56
	$b_{k,1}$ (mm)	10.3
	$a_{k,2}$	16.0
	$b_{k,2}$ (mm)	3.67
	c_k	2.23

of the total identified irradiance and its focal point corresponds to the intersection of the three laser beam axes.

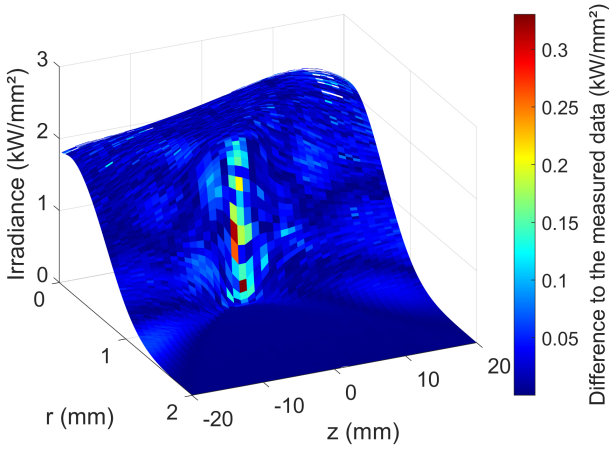

Figure 8: Identified laser model with difference to the measured data for $P = 4\,\mathrm{kW}$

3.2. Laser head identification

Since the established model is validated for the original laser beam, an experiment is designed to test if the three beams of the laser head can be considered as identical beams angled to the head axis. To compare experimental results and simulations, a series of laser shots were realized to obtain several marks corresponding to the zones impacted by the lasers. As the objective is to identify the geometrical limits of the beams independently of the laser power, a painted glass plate is chosen as a substrate. This material reduces the effect of conduction compared to metal, and the lower energy required to mark the substrate matches an ideal instantaneous shot more closely. Moreover, the obtained marks have a clear outline due to the removal of the paint, which leads to a better identification than the limit of the heat-affected zone on a metal. 14 shots were performed with a power of 400 W during 7 ms and a working distance variation step of 0.5 mm. The glass plate was then observed using a microscope to measure the size of the marks. The results shown in Fig. 9 indicate that while the spot can be considered as a circle near the focal point, an increase in working distance leads to a trefoil shape which cannot be represented by a single laser beam but is coherent with the proposed model (Fig. 6).

The model and results can be compared under the hypothesis that the observed mark corresponds only to the zone impacted by the laser, independently of the laser power. The validity of this hypothesis is studied during another experiment (Fig. 10). It is considered true as the energy used during the shots is minimal, reducing the possible effects of power variations to their minimum. Simulation results are superposed on the laser spots as a blue line (Fig. 9). This simulation uses 3 beams identical to the identified one and equally distributed on a cone so that each laser axis is at a 20° angle to the laser head vertical axis. Comparing the results reveals that both the size of the mark and its shape vary between simulation and experiments, with the shape of the predicted spot being correct when close to the focal point, but varying when the working distance increases. These differences can be explained by an overestimation of the angle between the beams and the wire axis. Fig. 6 represents the separation from a single spot to three spots as the working distance varies, and this effect is amplified by considering a bigger angle between the beams. This is observed at 3.1 mm, where the simulation shows distinct laser spots with a zone without power in the center, while the experimental mark has a shape representative of the three beams but forming a continuous contour at the same distance. For 4.6 mm all the beams create distinct marks and the simulation also results in three separated spots but they are further away from the center than the experimental results. Therefore, the angle of 20° considered for the simulation is likely higher than the actual angle, which needs to be identified on the experimental setup. However, the sizes of the predicted spots and the observed marks match well when the spots are separated, with the predicted and measured diameters being similar indicating a correct simulation of the individual beam behaviour. The simulation predicts lower sizes when the beams form only one mark with a single con-

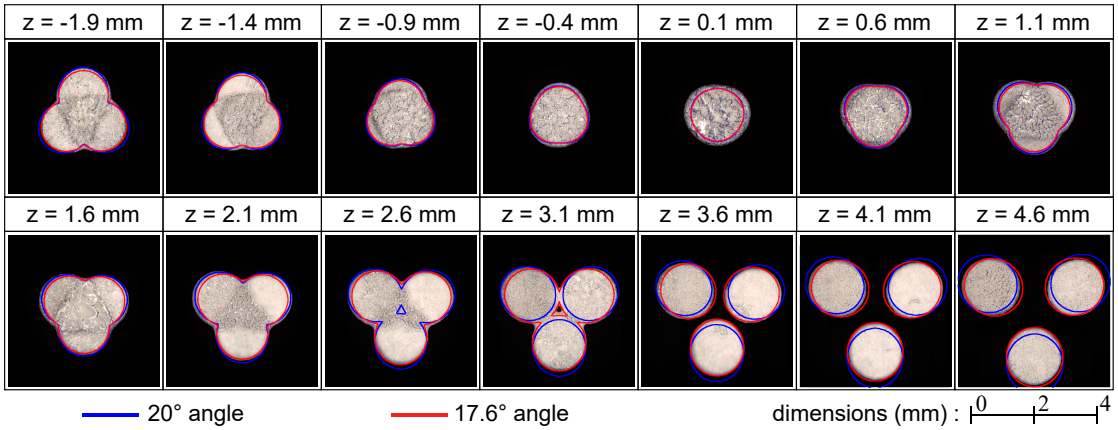

Figure 9: Laser shots on a painted glass plate for varying working distance with results of laser spot simulations for two models

tour, which challenges the hypothesis that the observed spot is only dependant on the beam width as it seems to be dependant on the energy density.

Another experiment is carried out to highlight the link between mark size and laser energy as well as to identify the angle between the beams. The protocol consists of three centred laser shots with working distances of −9, 0, and 9 mm, creating seven marks with the same centre. This result was repeated with shots of 400 W and a duration of 12, 15, 20 and 50 ms. The results (Fig. 10) indicate that the appearance of the mark size changes with the amount of energy and that its size increases slightly. Therefore the laser marks do not depend only on the beam width but can be considered as representative of its evolution. The laser energy during the shots is therefore kept at a minimum value to reduce this effect.

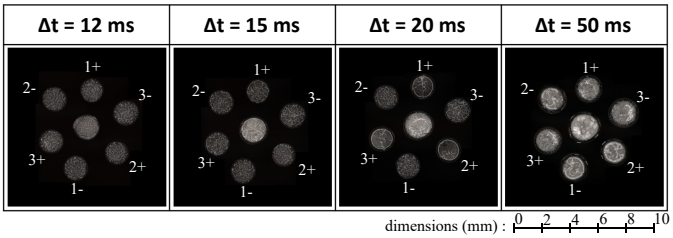

Figure 10: Laser spots for 3 centred shots with different working distances and 4 shot durations.

In order to determine the angle between the beams and the head vertical axis, each center of the shots is identified and each pair of opposite spots for +9 mm and −9 mm are linked by a line. This line materializes the beam axis and is used to measure its angle. All beams are supposed to have the same angle to the head axis, so using this method leads to an identified angle of 17.6°±0.2. This angle is then used in the power density simulation to obtain the laser spot contours displayed in red on Fig. 9. This identified angle leads to an improved prediction of the shape, as the transition from single to separate spots is well represented. Moreover, the distance between individual spots is similar to the one observed. However, while the spot size is still similar for individual spots, the simulation is systematically smaller when the beams create a single spot. This difference can be caused by the increase in energy density, as observed for the marks with varying duration showing an increase in size (Fig. 10).

With the proposed model of the source and the identified head parameters, the method of section 2 can be applied to simulate the power densities on any surface. Comparing the results obtained by this approach to an equivalent single Gaussian beam on a substrate with a working distance of −2 mm reveals that considering a single heat source cannot represent the trefoil shapes observed in Fig. 9. Moreover, the single beam model tends to overestimate the power at the centre of the spot by more than 15% compared to the identified model.

4. Process modelling

The three beams irradiance model presented before was mostly applied to simulate the power input on a part's surface, which corresponds more to a laser engraving context than additive manufacturing. Indeed, the laser is not only used to bring power to the part but to melt the wire and the part, forming a bead which will be the surface mostly impacted by the laser. Therefore, the wire and bead have to be included in the simulation of laser power to better represent the process behaviour. This section presents the model used to simulate how the wire can modify the power input on itself and other surfaces, and how the bead has been included with a model based on the bead shape.

4.1. Wire modelling

To simulate the irradiance on the wire, the first step is to model its geometry. The wire is considered to be a perfect cylinder with a radius of 0.6 mm. A discretization of this geometry into a point cloud with normals allows us to use the same method as before (section 2.2) to simulate the irradiance on the wire (Fig. 11). However, some configurations of the wire can lead to hidden zones, as the wire can block the path of the beams, especially when the intersection of the three beams is above the surface. The visibility of each surface point for each beam is taken into account by the variable v_i in Eq. 7, which is equal to 1 for visible points and 0 for unseen points. Several methods can be used to determine which points are hidden [33, 34], and the following paragraphs will present the chosen one and its results.

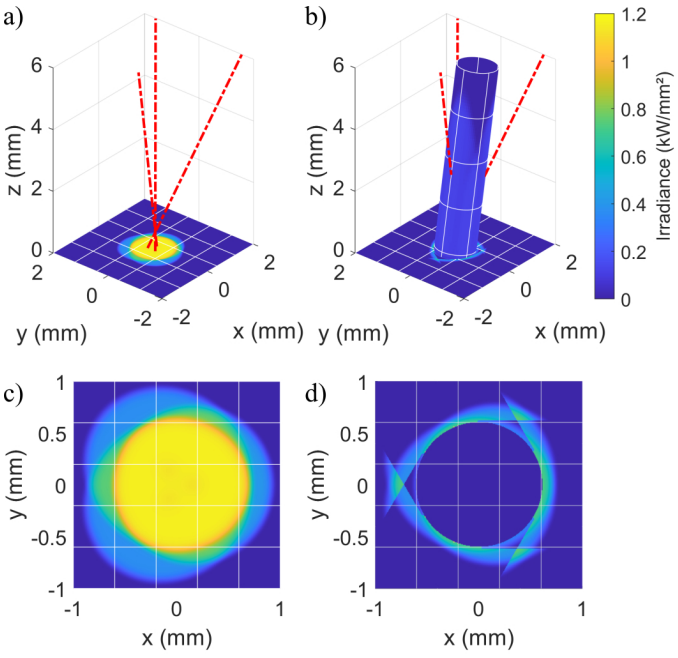

Figure 11: Simulation without (a and c) and with the wire (b and d) at a working distance of 0.5 mm and a head inclination of 10°

The chosen method for visibility computing considers a set of points $\mathbf{P}$ for the m surfaces $\mathbf{S}_j$ considered (Eq. 15).

$$\mathbf{P} = \{\mathbf{M} : \mathbf{M} \in \mathbf{S}_j \ , \ j \in [\![1 \ , \ m]\!]\} \tag{15}$$

Because all normals are outer-pointing, all points with a normal along the propagation direction of a beam are back-facing and therefore unseen by this beam. Since each beam propagates along the $-\mathbf{z}$ vector of their $\mathcal{R}_{Li}$ frame, the back-face points set $\mathbf{P}^i_{\mathrm{B}}$ for each beam is identified using the point normal in the beam frame (Eq. 16). Fig. 12 displays wire and substrate points in a beam frame with the identified back-points.

$$\mathbf{P}^i_{\mathrm{B}} = \{\mathbf{M} \in \mathbf{P} \ : \ {}^{\mathrm{Li}}w_{\mathrm{M}} < 0\} \tag{16}$$

Other points can be unseen while they are not back-facing because they are occluded by other surfaces. The occluding points can be considered as part of the back-face points. Under the hypothesis that locally all laser rays are assumed to be parallel, a point $\mathbf{M}$ is occluded by a back-face point $\mathbf{B}$ if they are aligned along the $-\mathbf{z}_{\mathrm{Li}}$ axis and if ${}^{\mathrm{Li}}z_{\mathrm{M}} < {}^{\mathrm{Li}}z_{\mathrm{B}}$. The ensemble of occluded points by of each point $\mathbf{B}$ of $\mathbf{P}^i_{\mathrm{B}}$ is the set $\mathbf{P}^i_{\mathrm{O,B}}$.

The total occluded set $\mathbf{P}^i_{\mathrm{O}}$ for each beam i is then equal to the union of the cast-shadow sets $\mathbf{P}^i_{\mathrm{O,B}}$ for each back-face point $\mathbf{B}$ in $\mathbf{P}^i_{\mathrm{B}}$ (Fig. 12). The point set $\mathbf{P}^i_{\mathrm{U}}$ consists of all unseen points for a laser beam i and is therefore equal to all back-face and occluded points. The visibility of all unseen points is equal to 0 (Eq. 18). Using this algorithm, the simulation can be corrected to obtain Fig. 11 without the overestimation in received power.

$$\mathbf{P}^i_{\mathrm{U}} = \mathbf{P}^i_{\mathrm{B}} \cup \bigcup_{B \in \mathbf{P}_{\mathrm{B}}} \mathbf{P}^i_{\mathrm{O,B}} \tag{17}$$

$$\forall \ \mathbf{M} \in \mathbf{P}^i_{\mathrm{U}} : \quad v_i(\mathbf{M}) = 0 \tag{18}$$

$$\forall \ \mathbf{M} \in \mathbf{P} \backslash \mathbf{P}^i_{\mathrm{U}} : \quad v_i(\mathbf{M}) = 1 \tag{19}$$

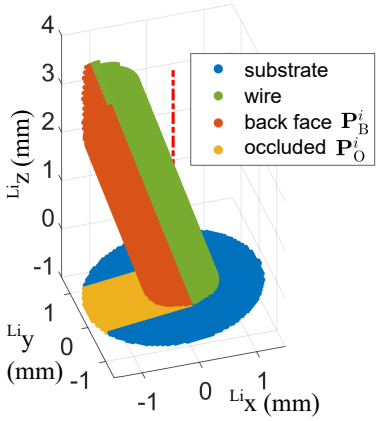

Figure 12: Visualisation of the different zones to determine the visibility for one beam

To check the hypothesis and verify the validity of the model, further laser shots are carried out on the glass plate, with the wire placed in contact with the substrate at different working distances. The laser spots are then photographed to observe the different shapes (Fig. 13). The resulting marks are similar to the ones observed in Fig. 9 but are incomplete, which can be explained by two effects. Because the wire touches the substrate during the shots, the zone of the substrate in contact with the wire will not receive any irradiance. This results in a circular area inside the spot which will not receive any power, which can be seen in the negative values of z. For the positive values of z, a second effect is observed and combined with the first one. This effect is the cast shadow from the wire, which results in a zone without power. It is only visible when the substrate is placed under the focal plane, as the beams need to interact with the wire before interacting with the substrate to cast a shadow. This results in rectangular-shaped shadows, as displayed in Fig. 12. The resulting marks can be compared to the simulated irradiance at the same working distances with a centred or off-centred wire.

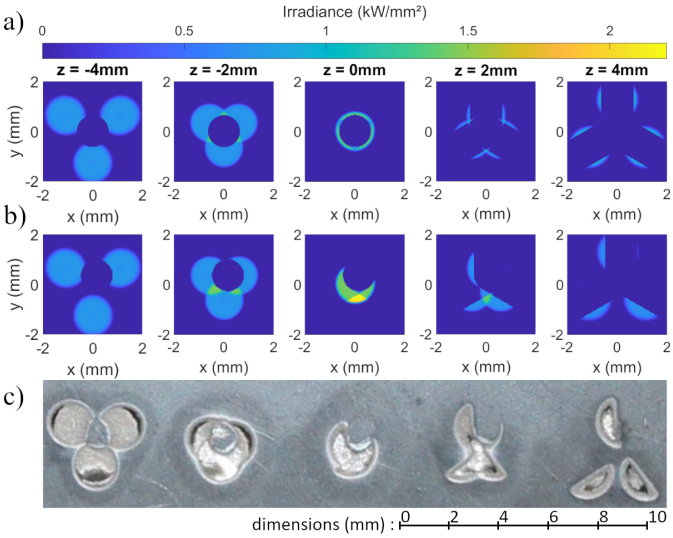

Figure 13: Comparisons between simulations of the irradiance with centred wire (a), off-centre wire (b), and photography with actual off-centred wire (c) for working distances of -4, -2, 0, 2, and 4 mm from left to right

Indeed, the nominal case corresponds to a centred wire, meaning that the axis of the wire corresponds to the vertical axis of the head. In the experimental setup, the wire axis can be adjusted to be on or off-centre from the beams. As the simulation is able to take both cases into account, the spots for a centred wire (Fig. 13a) and off-centred wire (Fig. 13b) can be compared to the experimental results. The shapes observed for the centred wire clearly highlight the two effects presented before, with a circular non-affected zone in the center combined with three rectangular-shaped shadows for $z > 0$. A translation of 0.15 mm along $\vec{x}$ and 0.35 mm along $\vec{y}$ (Fig. 13b) matches the shapes of the experimental marks (Fig. 13c). The wire position can then be adjusted accordingly on the experimental setup to centre the wire on the spots. These observations validate the efficiency of this model to represent realistic configurations of the wire, the substrate, and the laser beams.

4.2. Bead modelling

However, while the wire and substrate are present at the beginning of the weld, the process creates a bead which interacts with the laser. The interaction of the beams with this geometry leads to different irradiance values than when interacting on a plane or the wire, as each point of the bead will be at a different height and angle to the beam compared to the substrate. Therefore, modelling this geometry will complete the model and increase its accuracy and fidelity for power estimation. To represent the geometry of the bead front, which is the part interacting mostly with the laser, an approximation of the solidified bead profile is chosen according to models from the literature. This profile is first identified for multiple cross-sections, and then rotated along the $\vec{z}$ axis of the part to join the profiles at the front of the bead.

Beads are produced using IN718 wire on a S235-J steel substrate (Fig 14), with a working distance of -2 mm, laser power of 2.2 kW, wire feed speed of 2 m/min and travel speed of 1 m/min. An in-situ Keyence LJX8200 optical scanner is used to measure the beads on their entire length of 58 mm, leading to the mean profile with a 95% confidence interval represented in full and dashed blue lines on Fig. 15. A parabolic model is then used to describe the geometry, as it fits correctly inside the measured interval. Table 2 displays the dimensions of the bead as measured on the profile and the corresponding values for the identified parabolic model. With this model to describe the profile and approximate the bead, the coordinates of each point and its associated normal are known, as required for the simulation.

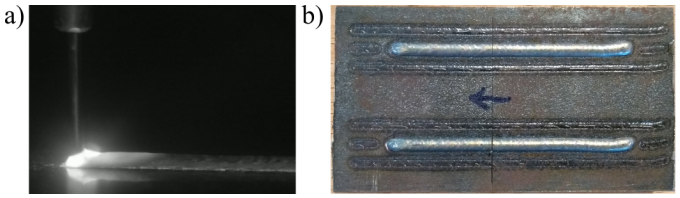

Figure 14: Photography of the bead during manufacturing (a) and substrate with beads (b)

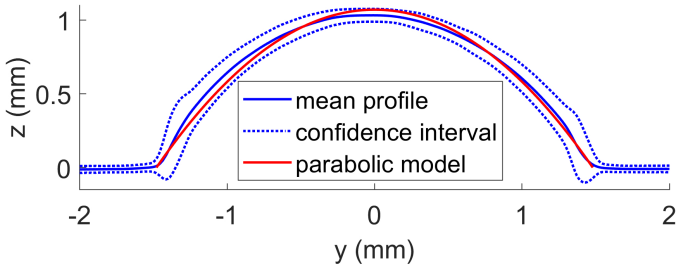

Figure 15: Measured average profile for a bead with confidence interval, compared to the identified parabolic model

Adding the model developed in section 4.1, an in-process configuration including both bead and wire can be simulated to estimate the power density on different surfaces. Simulation results (Fig. 16) indicate that laser power is mainly focused on the bead, getting 83% of the total power and a little on the wire with around 17%, while the substrate receives no irradiance. For a working distance of -2 mm, the laser spots remain separated, leading to a dependency on the head rotation to either have one or two spots at the front of the bead.

Table 2: Bead dimensions from measure and model

	width (mm)	height (mm)	area (mm²)
measured	2.90 ± 0.13	1.03 ± 0.04	2.13 ± 0.27
model	2.96	1.07	2.11

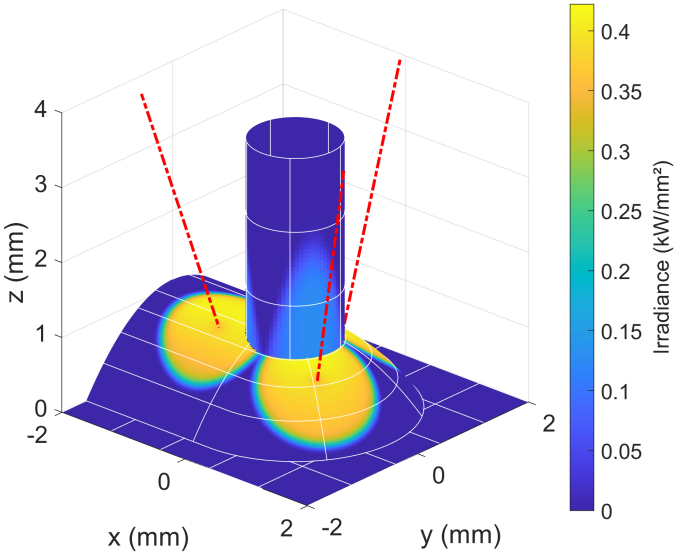

Figure 16: Irradiance on the wire and bead during the process, with a working distance of -2 mm

5. Application to the head rotation influence

Among the parameters which influence power density, the position and orientation of the head relative to the substrate should be taken into account. Not only can specific values be chosen during process planning to modify power density, but also variations of these parameters can be observed during manufacturing. For example, an inadequate estimation of bead height during the manufacturing of layers leads to a varying working distance, whose influences on power density is illustrated in Fig. 6. For a working distance of -2 mm, these laser power simulations indicate that the three beams lead to three distinct spots. Because of these separated spots, a rotation of the head about its vertical axis changes the layout of the spots relative to the travel direction. Furthermore, this rotation does not change the wire position if it is centred, and has little effect on the power delivered to the wire. To indicate if this parameter has an effect on bead geometry, several beads are produced with varying values of the head rotation angle α.

Fig. 17 presents three cross-sections of beads with their values of α corresponding to specific configurations of the laser spots relative to travel direction: a symmetrical configuration with one laser at the front of the bead and two at the back ($\alpha = -30°$); an asymmetrical configuration with two lasers on one side ($\alpha = 60°$); and another asymmetrical configuration with two lasers on the other side ($\alpha = 0°$). Using the same parameters as in section 4.2, all beads are produced along the $+\vec{x}$ direction. They are measured with the Keyence optical scanner to determine the mean outer profile with its position relative to the programmed trajectory. Additionally, each bead is cut in the centre of the path to obtain the cross-sectional profiles and evaluate the penetration. It can be observed that while the asymmetrical configurations lead to asymmetrical beads with deep penetrations, the symmetrical configuration presents a more symmetrical bead with a shallow penetration.

To characterize how the head rotation affects the power density, the three configurations are simulated using the irradiance model. In order to better illustrate the link between power density and geometry, measurements of each bead are used to obtain the irradiance directly on representative surfaces. To model the outer surface of the bead, the mean profiles for each configuration, represented as blue outlines on Fig. 17, are extruded along the $\vec{x}$ axis. This geometry representing the front and back of the bead with the same model deviates from the process configuration presented in the previous section. Still, it reduces the problem to a two-dimensional model to obtain comparable data to the cross-sections. Knowing the position of the beads relative to the programmed trajectory, the laser beams are placed so that the beams central axis is centred on the trajectory. The irradiance on the surface is simulated, as displayed at the top of Fig. 17. The use of an extruded beam instead of a model including the front introduces variations in the simulated irradiance and reduces the sensitivity to the travel direction, as considering a production along the $+\vec{x}$ or $-\vec{x}$ directions would result in the same simulated power densities. However, considering this 2D problem results in a one-dimensional representation of laser power, which can then be compared to the cross-sections of the beads. To obtain this representation, the laser power is summed along the path travelling direction to compute a linear power density on the bead, represented in red in Fig. 17. The chosen representation displays the power density dI_ℓ in kW/mm on the profile along its normal vectors.

The first observation is that the limit of power density on the right corresponds to the bead limit, meaning that the lasers interact mostly with the beads and not the substrate, as observed in section 4.2 for nominal geometries. Furthermore, the asymmetrical configurations show a displacement of the bead relative to the penetration. Linking this displacement to the asymmetrical power profile reveals that the direction corresponds to where the power density is lowest. As for the symmetrical configuration, the bead position and shape create a light asymmetry in power density with a little more power on the left. The

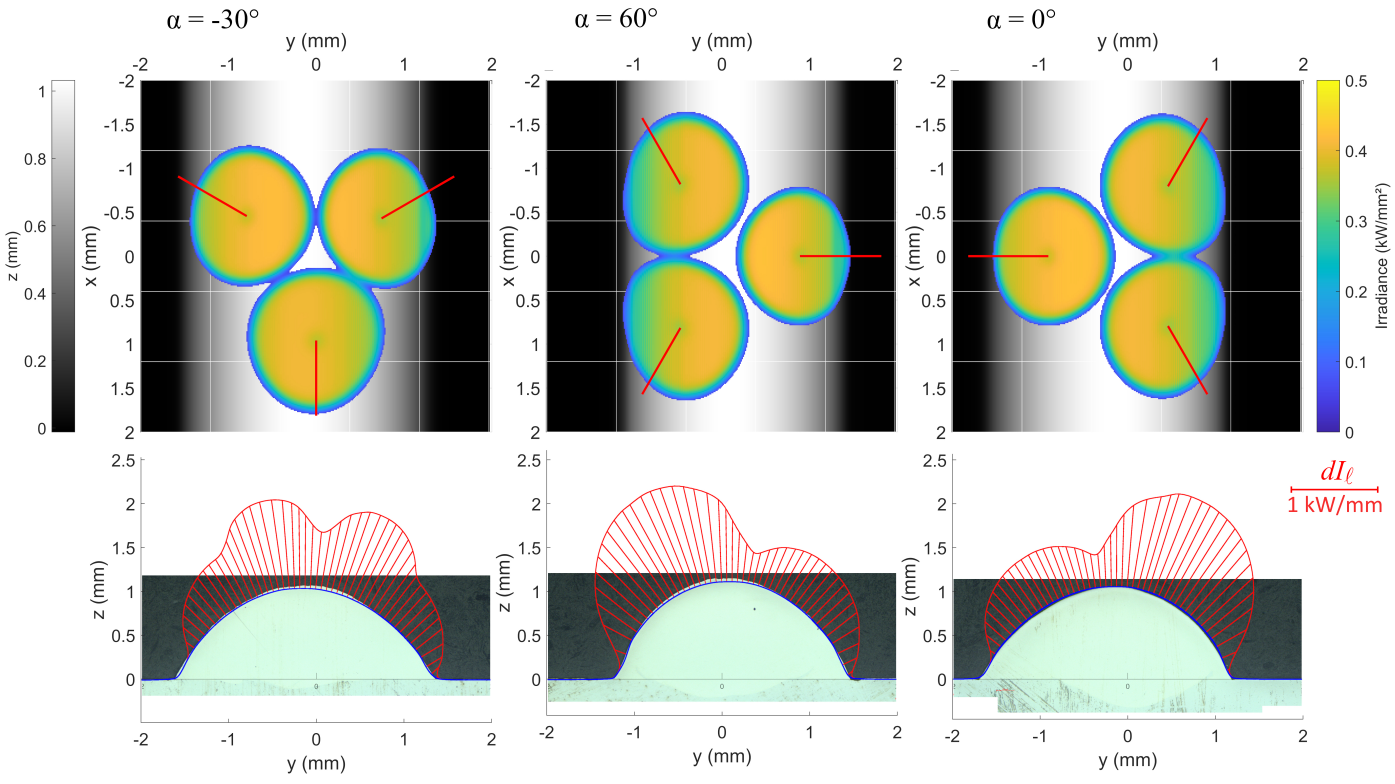

Figure 17: Beams positions and bead cross-sections for different values of head rotation with comparison to the simulated power density dI_ℓ

maximal power density is 1.03 kW/mm in this configuration, compared to 1.20 kW/mm and 1.19 kW/mm for the two asymmetrical configurations (middle and right). This means that the head rotation can modify the maximal value of the linear density by 17% compared to a symmetrical configuration. The penetration is shallower for the bead on the left, which also corresponds to the situation with a lower maximal value of power density. While the penetration is centred compared to the other ones, it shows a light offset to the left, which is also the side with the higher power density.

6. Conclusions and perspectives

The proposed approach for laser power simulation can be used for any number of beams on any surface and is applied to simulate the power density on process-characteristic surfaces: the substrate, bead and wire. A model for the laser beam power is proposed based on beam measurement data and is used to represent the behaviour of the three beams coaxial head used in the experimental setup. Comparing the simulated laser spots and experimental results reveals that the proposed approach can predict the shapes and sizes of laser spots in various configurations. To simulate the power in process configurations, both the wire and bead are modelled and the received laser power on these surfaces is estimated. At a working distance of −2 mm, it is observed that the bead receives most of the power, the wire a little, and the substrate none. The predicted spots on the bead are distinct with one spot for each beam. The head rotation varies the disposition of these spots relative to the travel direction, resulting in variations in the power density profile. Some values of head rotation result in symmetrical power density profiles, while others generate asymmetrical ones. Beads produced in these configurations are also found to have varying geometries, with symmetrical beads for symmetrical power densities and asymmetrical geometries for asymmetrical densities. Moreover, a relative displacement of the beads to their penetration profiles is observed, while the penetration depth is higher for configurations generating a higher maximum of the power density profile.

While the proposed model is compared to experimental results for spot sizes and shapes, a comparison of the estimated and measured power densities for different working distances would further validate the model. The models used to describe the wire and bead geometries could be improved to better take into account some of their properties, such as the possible wire curvature. The observed bead asymmetry could also be modelled to more accurately describe the bead geometry but would require using two second order or a higher order polynomial functions.

While this article focused on irradiance, the absorbed power is essential in process simulation. Using a constant absorptivity depending on the material and laser properties proves to be a reasonable assumption to determine the absorbed power densities from the simulated irradiance. This will not change the conclusions on the spots' shapes and sizes but will add a coefficient to the estimated values. Because the incidence angle for each point of the surface is computed in the developed method, the estimation of the absorbed power densities could be further improved by considering an absorptivity dependent on the incidence angle.

This model can also be used in different configurations to estimate the effect of head positioning parameters, such as varying working distances or head orientations. While this paper focused on the effect on the geometries, further studies could investigate the influence on the microstructure. The power densities can also be simulated for different sets of process parameters which could predict process defects and adapt manufacturing recipes. The link to internal and external bead geometry could be further investigated and extended to bead overlapping and layer manufacturing in order to propose adapted trajectories and manufacturing strategies.

7. Acknowledgement

The authors gratefully acknowledge the technical support provided by the Paris-Saclay Additive Manufacturing Platform funded by Université Paris-Saclay and École normale supérieure Paris-Saclay through the strategic research initiative program (ANR-11-IDEX-0003-02).

References

[1] ISO/ASTM 17296-2, Additive manufacturing — General principles — Part 2: Overview of process categories and feedstock, Standard, 2015.

[2] D. Ding, Z. Pan, D. Cuiuri, H. Li, Wire-feed additive manufacturing of metal components: technologies, developments and future interests, The International Journal of Advanced Manufacturing Technology 81 (2015) 465–481. doi:10.1007/s00170-015-7077-3.

[3] M. Motta, A. G. Demir, B. Previtali, High-speed imaging and process characterization of coaxial laser metal wire deposition, Additive Manufacturing 22 (2018) 497–507. doi:10.1016/j.addma.2018.05.043.

[4] A. Ayed, G. Bras, H. Bernard, P. Michaud, Y. Balcaen, J. Alexis, Study of arc-wire and laser-wire processes for the realization of Ti-6Al-4V alloy parts, MATEC Web of Conferences 321 (2020). doi:10.1051/matecconf/202032103002.

[5] F. Du, J. Zhu, X. Ding, Q. Zhang, H. Ma, J. Yang, H. Cao, Z. Ling, G. Wang, X. Duan, S. Fan, Dimensional characteristics of Ti-6Al-4V thin-walled parts prepared by wire-based multi-laser additive manufacturing in vacuum, Rapid Prototyping Journal 25 (2019) 849–856. doi:10.1108/RPJ-08-2018-0207.

[6] M. Bambach, I. Sizova, F. Kies, C. Haase, Directed energy deposition of Inconel 718 powder, cold and hot wire using a six-beam direct diode laser set-up, Additive Manufacturing 47 (2021) 102269. doi:10.1016/j.addma.2021.102269.

[7] T. E. Abioye, J. A. Folkes, A. T. Clare, A parametric study of Inconel 625 wire laser deposition, Journal of Materials Processing Technology 213 (2013) 2145–2151. doi:10.1016/j.jmatprotec.2013.06.007.

[8] A. G. Medrano-Tellez, Fibre laser metaldeposition with wire: parameters study and temperature control, Ph.D. thesis, University of Nottingham, 2010.

[9] J. Xiong, G. Zhang, H. Gao, L. Wu, Modeling of bead section profile and overlapping beads with experimental validation for robotic GMAW-based rapid manufacturing, Robotics and Computer-Integrated Manufacturing 29 (2013) 417–423. doi:10.1016/j.rcim.2012.09.011.

[10] W. Aiyiti, W. Zhao, B. Lu, Y. Tang, Investigation of the overlapping parameters of MPAW-based rapid prototyping, Rapid Prototyping Journal 12 (2006) 165–172. doi:10.1108/13552540610670744.

[11] A. Sharma, N. Arora, B. Mishra, Mathematical model of bead profile in high deposition welds, Journal of Materials Processing Technology 220 (2015) 65–75. doi:10.1016/j.jmatprotec.2015.01.009.

[12] Y. Cao, S. Zhu, X. Liang, W. Wang, Overlapping model of beads and curve fitting of bead section for rapid manufacturing by robotic MAG welding process, Robotics and Computer-Integrated Manufacturing 27 (2011) 641–645. doi:10.1016/j.rcim.2010.11.002.

[13] G.-H. Kim, S.-I. Kang, S.-B. Lee, Study on the estimate of weld bead shape and the compensation of welding parameters by considering weld defects in horizontal fillet welding, 2000, pp. 212–216. doi:10.1109/KES.1999.820157.

[14] S. Suryakumar, K. K.P., A. Bernard, U. Chandrasekhar, R. Nadella, D. Sharma, Weld bead modeling and process optimization in hybrid layered manufacturing, Computer-Aided Design 43 (2011) 331–344. doi:10.1016/j.cad.2011.01.006.

[15] M. R. Kumar, S. Suryakumar, A. Sharma, Bi-polynomial fourth-order weld bead model for improved material utilization and accuracy in wire-arc additive manufacturing: A case of transverse twin-wire welding, Advances in Industrial and Manufacturing Engineering 2 (2021) 100049. doi:10.1016/j.aime.2021.100049.

[16] D. Ding, Z. Pan, D. Cuiuri, H. Li, A multi-bead overlapping model for robotic Wire and Arc Additive Manufacturing (WAAM), Robotics and Computer-Integrated Manufacturing 31 (2015) 101–110. doi:10.1016/j.rcim.2014.08.008.

[17] V. Cazaubon, A. Abi Akle, X. Fischer, A parametric study of additive manufacturing process: TA6V laser wire metal deposition, in: Advances on Mechanics, Design Engineering and Manufacturing III: Proceedings of the International Joint Conference on Mechanics, Design Engineering & Advanced Manufacturing, JCM 2020, June 2-4, 2020., Cham: Springer International Publishing, 2021, pp. 15–20. doi:10.1007/978-3-030-70566-4_4.

[18] S. H. Mok, G. Bi, J. Folkes, I. Pashby, Deposition of Ti-6Al-4V using a high power diode laser and wire, part I: Investigation on the process characteristics, Surface and Coatings Technology 202 (2008) 3933–3939. doi:10.1016/j.surfcoat.2008.02.008.

[19] S. Ocylok, M. Leichnitza, S. Thiemeb, S. Nowotny, Investigations on laser metal deposition of stainless steel 316L with coaxial wire feeding, in: 9th International Conference on Photonic Technologies (LANE 2016), volume 83 of *Physics Procedia*, Elsevier Procedia, 2016.

[20] S. Ji, F. Liu, T. Shi, G. Fu, S. Shi, Effects of defocus distance on three-beam laser internal coaxial wire cladding, Chinese Journal of Mechanical Engineering 34 (2021) 45. doi:10.1186/s10033-021-00560-9.

[21] C. Hagenlocher, P. O'Toole, W. Xu, M. Brandt, M. Easton, A. Molotnikov, Analytical modelling of heat accumulation in laser based additive manufacturing processes of metals, Additive Manufacturing 60 (2022) 103263. doi:10.1016/j.addma.2022.103263.

[22] Z. Nie, G. Wang, J. D. McGuffin-Cawley, B. Narayanan, S. Zhang, D. Schwam, M. Kottman, Y. K. Rong, Experimental study and modeling of H13 steel deposition using laser hot-wire additive manufacturing, Journal of Materials Processing Technology 235 (2016) 171–186. doi:10.1016/j.jmatprotec.2016.04.006.

[23] J. Goldak, A. Chakravarti, M. Bibby, A new finite element model for welding heat sources, Metallurgical Transactions B 15 (1984) 299–305. doi:10.1007/BF02667333.

[24] H. Wei, F. Liu, W. Liao, T. Liu, Prediction of spatiotemporal variations of deposit profiles and inter-track voids during laser directed energy deposition, Additive Manufacturing 34 (2020) 101219. doi:10.1016/j.addma.2020.101219.

[25] F. Liu, L. Wei, S. Shi, H. Wei, On the varieties of build features during multi-layer laser directed energy deposition, Additive Manufacturing 36 (2020) 101491. doi:10.1016/j.addma.2020.101491.

[26] V. Cazaubon, Additive manufacturing process by molten wire deposition : model, methods and strategies for the correction of mechanical part defects, Ph.D. thesis, Université de Bordeaux, 2021.

[27] H. Liu, Y. Zhou, An interaction model for laser and powder in wide-beam laser cladding, The International Journal of Advanced Manufacturing Technology 112 (2021) 15–23. doi:10.1007/s00170-020-06330-6.

[28] H. Sakamoto, K. Shibata, F. Dausinger, Laser welding of different aluminum alloys, International Congress on Applications of Lasers & Electro-Optics 1992 (1992) 523–528. doi:10.2351/1.5058523.

[29] K. H. Leong, H. K. Geyer, K. R. Sabo, P. G. Sanders, Threshold laser beam irradiances for melting and welding, Journal of Laser Applications 9 (1997) 227–231. doi:10.2351/1.4745464.

[30] K. H. Leong, H. K. Geyer, Laser beam welding of any metal, International Congress on Applications of Lasers & Electro-Optics 1998 (1998) F242–F250. doi:10.2351/1.5059176.

[31] M. Froend, V. Ventzke, N. Kashaev, B. Klusemann, J. Enz, Thermal analysis of wire-based direct energy deposition of Al-Mg using different laser irradiances, Additive Manufacturing 29 (2019) 100800. doi:10.1016/j.addma.2019.100800.

[32] A. E. Siegman, How to (maybe) measure laser beam quality, in: M. Dowley (Ed.), DPSS (Diode Pumped Solid State) Lasers: Applications and Issues, volume 17 of *OSA Trends in Optics and Photonics*, Optical Society of America, Washington, D.C., 1998. doi:10.1364/DLAI.1998.MQ1.

[33] J.-M. Hasenfratz, M. Lapierre, N. Holzschuch, F. Sillion, A survey of real-time soft shadows algorithms, Computer Graphics Forum 22 (2003) 753–774. doi:10.1111/j.1467-8659.2003.00722.x.

[34] T. Ritschel, C. Dachsbacher, T. Grosch, J. Kautz, The state of the art in interactive global illumination, Computer Graphics Forum 31 (2012) 160–188. doi:10.1111/j.1467-8659.2012.02093.x.